Bulletin of the Seismological Society of America, Vol. 108, No. 2, pp. 690–701, April 2018, doi: 10.1785/0120170207

Ⓔ

# Examining the Capability of Statistical Models to Mitigate Induced Seismicity during Hydraulic Fracturing of Shale Gas Reservoirs

by James P. Verdon and Jessica Budge

**Abstract** Injection into the subsurface is carried out by industry for a variety of reasons, for example, storing wastewater, enhanced oil recovery, and hydraulic fracture stimulation. By increasing subsurface pressures, injection can trigger felt seismicity (i.e., sufficient magnitude to be felt at the surface) on pre-existing faults. As the number of cases of felt seismicity associated with hydraulic fracturing (HF) has increased, strategies for mitigating induced seismicity are required. However, most hydraulic stimulation activities do not induce felt seismicity. Therefore, a mitigation strategy is required that is capable of differentiating the normal case from abnormal cases that trigger larger events. In this article, we test the ability of statistical methods to estimate the largest event size during stimulation, applying these approaches to two datasets collected during hydraulic stimulation in the Horn River Shale, British Columbia, where HF was observed to reactivate faults. We apply these methods in a prospective manner, using the microseismicity recorded during the early phases of a stimulation stage to make forecasts about what will happen as the stage continues. We do so to put ourselves in the shoes of an operator or regulator, where decisions must be taken based on data as it is acquired, rather than a *post hoc* analysis once a stimulation stage has been completed. We find that the proposed methods can provide a reasonable forecast of the largest event to occur during each stage. This means that these methods can be used as the basis of a mitigation strategy for induced seismicity.

*Electronic Supplement:* Simulated $M_{\mathrm{MAX}}^{\mathrm{M}}$ values for each injection stage.

## Introduction

### Hydraulic Fracturing-Induced Seismicity

Any human activity that alters the stress state in the Earth's crust has the potential to induce seismic activity. Induced seismicity has been associated with mining (e.g., Li *et al.*, 2007), impounding reservoirs (e.g., Gupta, 1985), conventional oil and gas extraction (e.g., Segall, 1989), and subsurface fluid injection, whether for hydraulic fracturing (HF; e.g., Bao and Eaton, 2016), disposal of waste fluids (e.g., Keranen *et al.*, 2013), carbon capture and storage (e.g., Stork *et al.*, 2015), or geothermal energy (e.g., Häring *et al.*, 2008).

It has been conclusively demonstrated that injecting fluids into the subsurface can trigger seismicity, where increased pore-fluid pressures lead to the activation of critically stressed faults (e.g., Raleigh *et al.*, 1976). However, it should be noted that the overwhelming majority of such operations are not thought to cause earthquakes. Nevertheless, as the above practices have increased in scale and become more widespread, the issue of injection-induced seismicity has grown in significance.

Although much of the recent focus has been on wastewater disposal, several cases of HF-induced seismicity (HF-IS) have been identified (e.g., B.C. Oil and Gas Commission 2012, 2014; Clarke *et al.*, 2014; Darold *et al.*, 2014; Friberg *et al.*, 2014; Schultz, Mei, *et al.*, 2015; Schultz, Stern, *et al.*, 2015; Skoumal *et al.*, 2015; Atkinson *et al.*, 2016; Bao and Eaton, 2016; Wang *et al.*, 2016). It is vital that our understanding of HF-IS improves such that industrial operators are capable of mitigating against triggering seismic activity. However, for many of these case examples monitoring arrays were not deployed until after large events had occurred, or available monitoring arrays consisted solely of regional networks, where the nearest station may have been many kilometers from the site. This means that there is often little useful data that can be used to study the processes that happened in the lead-up to these events, and thereby which mitigation steps might have been possible.

The number of cases of HF-IS is very small when compared with the overall number of wells that have been hydraulically stimulated. As such, any mitigation scheme should be capable of quickly differentiating the normal case, where HF does not cause fault reactivation leading to larger events, from the abnormal case where large events may be triggered, and therefore where mitigating strategies such as reducing injection volumes or ceasing injection altogether may be necessary.

### Mitigation of HF-IS

At present, where regulations pertaining to HF-IS have been applied, they take the form of traffic-light schemes (TLSs), whereby operators take actions based on the magnitude of events induced during operations. These schemes have the advantage of being relatively simple to administer and can be understood by the public. However, they are somewhat reactive in their nature (as opposed to proactive): an operational response is required, such as reducing or stopping injection, only after an event of a given size has occurred.

The purpose of this article is not to argue against the use of TLSs, which can play a useful role in the regulation of HF-IS. However, it is our view that, in addition to complying with TLS regulations, operators should seek to mitigate induced seismicity in a more proactive manner. If nothing else, operators will wish to ensure that they remain within the specified TLS thresholds during their operations because reaching "red lights" entails the imposition of operational constraints, and may also affect operator reputation and confidence with the public.

To take a proactive approach to HF-IS, operators must develop the capacity to model their activities, allowing them to make forecasts about the HF-IS that may occur as their operations continue. In the broadest sense, two types of modeling approaches are available: physical and statistical. Physical models aim to simulate the processes that occur during hydraulic stimulation, usually using numerical methods such as finite elements (e.g., Maxwell *et al.*, 2015), discrete elements (e.g., Yoon *et al.*, 2014), rate and state approaches based on modeled stress changes (e.g., Hakimhashemi *et al.*, 2014), or by resolving modeled stress changes onto pre-existing fault and fracture networks (e.g., Verdon *et al.*, 2015). However, such models often require extensive site characterization to identify and characterize both nearby faults and the local stress state. Such models also come with a significant number of free parameters that must be tuned to provide a reasonable representation of reality. As such they are better suited for understanding the physical processes that have occurred at a site *a posteriori*. For HF operators who might be required to manage induced seismicity in real time at a significant number of active well sites, simple models with a relatively small number of free parameters are required. In this respect, statistical models become more favorable.

Statistical approaches seek to characterize the observed seismic event population via a statistical model, usually the Gutenberg and Richter (1944) (hereafter, G-R) distribution. Such a model can then be extrapolated to estimate the event population that is expected to have occurred by the end of the injection period. Several such models have been proposed (e.g., Shapiro *et al.*, 2010; Hallo *et al.*, 2014; McGarr, 2014; van der Elst *et al.*, 2016).

These models are similar in their underlying assumptions: event magnitudes can be characterized by the G-R distribution, and the rate of seismicity is linked in some way to the injection volume. This relationship is then extrapolated based on recorded seismicity during the early stages of injection to estimate what the resulting event population would be once the total volume has been injected. From this estimated population, the largest event size can be forecasted. These models have the advantage that they require only a few parameters, which can be measured as operations progress. This makes them better suited for the task of providing *a priori* mitigation of induced seismicity.

Although these models have been tested at several sites (e.g., Hallo *et al.*, 2014; Hajati *et al.*, 2015), the crucial aspect investigated in this article is that we seek to apply these methods in a prospective manner (e.g., Langenbruch and Zoback, 2016). We do not apply these models using the overall event population that has been acquired during hydraulic stimulation in a *post hoc* manner. Instead, we put ourselves into the shoes of an operator or regulator, where forecasts must be made using only the data that has been acquired prior to a given point in time. Evidently, the underlying assumption for these methods is that the parameters used to characterize the seismicity as a function of injection volume remain unchanged during a given operation.

We apply these methods to two datasets collected during hydraulic stimulation in the Horn River Shale. These multiwell multistage sites were monitored using downhole microseismic arrays, producing very high-quality datasets. These datasets are described in the Datasets section, after which we describe the methods of Shapiro *et al.* (2010) and Hallo *et al.* (2014) in greater detail and apply them to the datasets.

## Datasets

In our case example, we examine microseismic datasets from two multiwell multistage HF treatments conducted in the Horn River Shale formation in British Columbia, Canada. The pads from which the two sets of wells were drilled are ~7 km apart from each other. In the following, we refer to the two datasets as HR1, which was completed in 2011, and HR2, which was completed in 2013. These datasets were provided by the operating company; they are proprietary and cannot be released to the public.

### HR1 Microseismic Data

A total of nine horizontal wells were drilled from the HR1 pad. A total of 146 stages were stimulated, with between 15 and 18 stages per well. Microseismic data were recorded by arrays of up to 100 three-component geophones placed in boreholes adjacent to those being stimulated (in both the vertical and horizontal sections of the wells). The

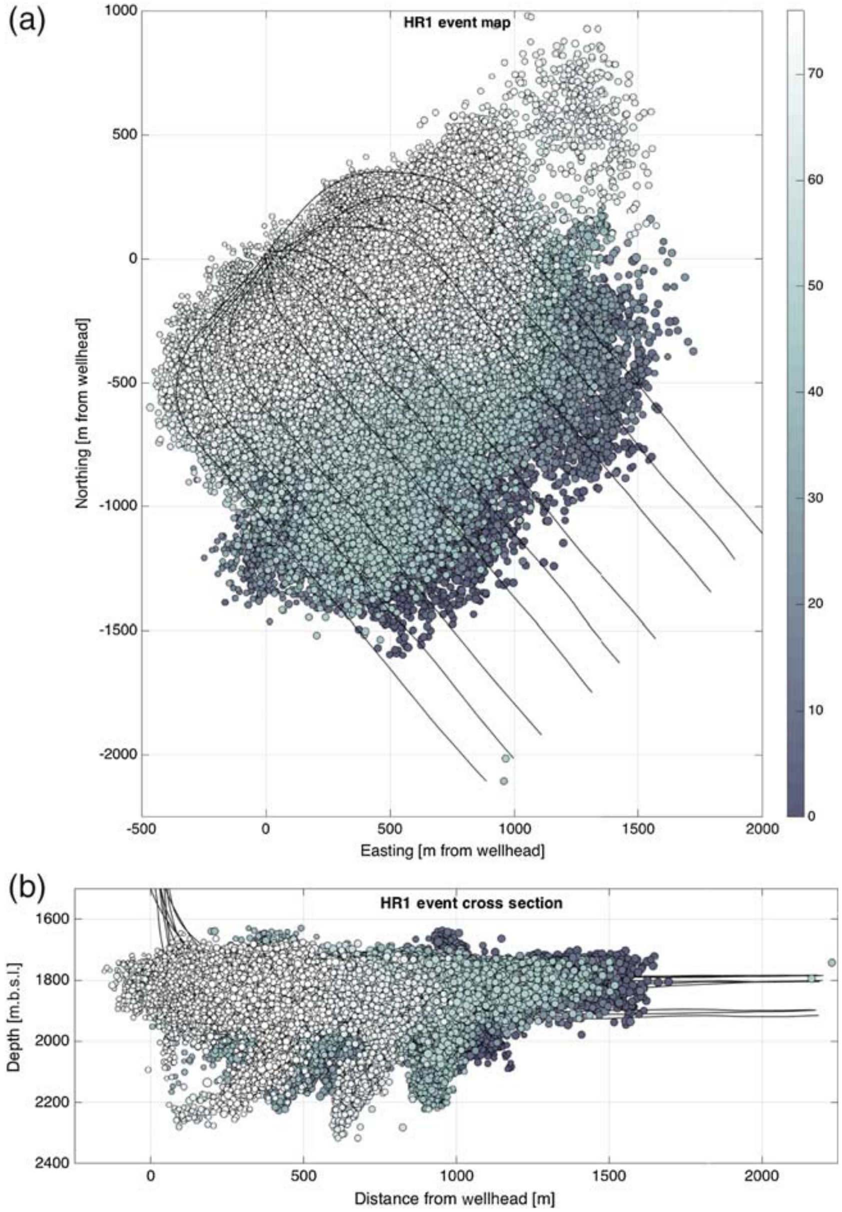


**Figure 1.** (a) Map and (b) cross-section views of microseismic events recorded during hydraulic fracturing (HF) at HR1. Events are shaded by the number of the stage with which they are associated. The black lines mark the horizontal wells. The color version of this figure is available only in the electronic edition.

positions of the geophones were varied as stimulation progressed along the wells, in at least 21 configurations.

Data were provided from 76 of the stages, consisting of a total of 140,100 events. These were the stages closest to the heels of the wells, and therefore closest to the monitoring arrays, where the best-quality microseismic data could be gathered. Events were located by inverting picked *P*- and *S*-wave arrival times through a layered anisotropic velocity model. A map and cross section of the HR1 microseismic events are shown in Figure 1. Event magnitudes were calculated by fitting an idealized source model to the event displacement spectra to determine the seismic moment (e.g., Stork *et al.*, 2014). Throughout this article, when referring to magnitude our implication is moment magnitude $M_w$. In both cases, this processing of the data was performed by a service provider, ESG Solutions.

### HR2 Microseismic Data

A total of 10 wells were drilled from the HR2 pad, 237 stages were stimulated, with between 23 and 24 stages per well. Microseismic data were recorded by an array of 96 three-component geophones placed in three adjacent boreholes. Data were provided from 119 stages, consisting of 92,700 events. As with the HR1 pad, data were provided for the stages nearest to the heels of the wells, where they are in closest proximity to the monitoring array (and therefore are expected to provide the best-quality data). A map and cross section of the HR2 events are shown in Figure 2.

In both case studies, examination of event locations reveals evidence for the interaction between HF and faults in the form of planar features extending downward into the underlying Keg River limestone formation. At HR1, the largest event has a magnitude $M_w$ 1.3, whereas at HR2 the largest event has a magnitude $M_w$ 0.5. In both cases, these magnitudes are larger than what is typically observed when hydraulic fractures propagate through shale gas reservoirs, where magnitudes are generally less than 0 (e.g., Maxwell *et al.*, 2010).

## Using Event Population Statistics to Forecast the Largest Event Size

We refer to $M_{\mathrm{MAX}}^{\mathrm{O}}$ as the largest magnitude event observed during a particular stage, and $M_{\mathrm{MAX}}^{\mathrm{M}}$ as the expected largest magnitude as estimated by a modeling strategy. Ideally, modeling strategies should aim to produce conservative estimates of $M_{\mathrm{MAX}}^{\mathrm{M}}$, such that $M_{\mathrm{MAX}}^{\mathrm{O}} \leq M_{\mathrm{MAX}}^{\mathrm{M}}$. Here, we examine the abilities of two published methods, Shapiro *et al.* (2010) and Hallo *et al.* (2014), to forecast $M_{\mathrm{MAX}}^{\mathrm{M}}$ during hydraulic stimulation.

### Seismogenic Index (Shapiro *et al.*, 2010)

Shapiro *et al.* (2010) define the seismogenic index $S_I$ as

$$S_I = \log_{10}\left(\frac{N_t(M)}{V_t}\right) + bM, \qquad (1)$$

in which $N_t(M)$ is the number of events that have occurred at time $t$ that are larger than a given magnitude $M$, $b$ is the G-R

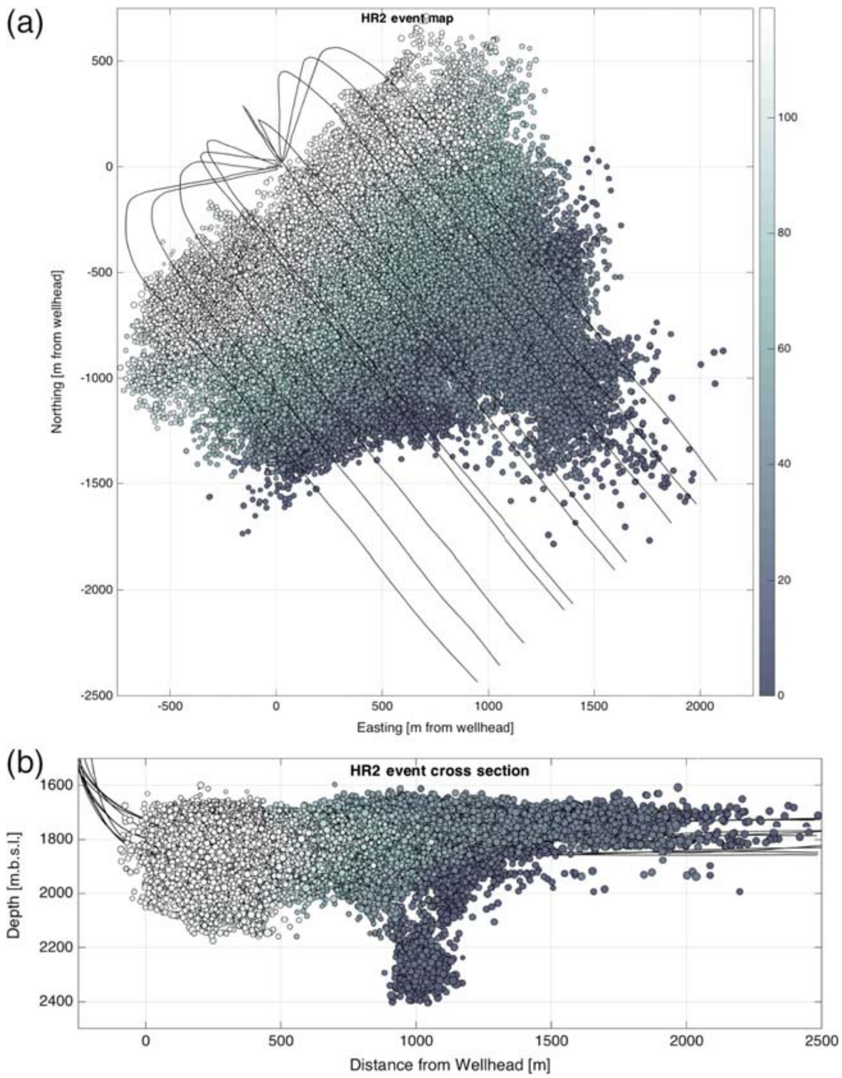


**Figure 2.** (a) Map and (b) cross-section views of microseismic events recorded during HF at HR2. Events are shaded by the number of the stage with which they are associated. The black lines mark the tracks of the horizontal wells. The color version of this figure is available only in the electronic edition.

$b$-value for the observed event magnitude distribution (EMD), and $V_t$ is the cumulative volume injected up until this time (note that Shapiro *et al.*, 2010, use $\Sigma$ to denote the seismogenic index; we use $S_I$ instead to differentiate with other uses of $\Sigma$ elsewhere in this article). Assuming that the number of events induced per unit volume injected does not change, then $S_I$ will be constant—constant $S_I$ has been observed by Dinske and Shapiro (2013) and van der Elst *et al.* (2016) for a wide range of cases studies. Shapiro *et al.* (2010) show that, in such an instance, if the occurrence of individual events can be treated as an independent Poisson process, then the probability that an event larger than $M$ does not occur if a total volume $V_T$ is injected can be calculated as

$$\mathbb{P} = \exp(-V_T \times 10^{S_I - bM}). \quad (2)$$

Rearranging this equation, we arrive at a forecast for the size of event that will not be exceeded, given a confidence level $\chi$:

$$M_{\mathrm{MAX}}^{\mathrm{M}} = \left(S_I - \log\left(\frac{-\ln(\chi)}{V_T}\right)\right)/b. \quad (3)$$

To provide a mitigation strategy, we are interested in establishing an upper bound for $M_{\mathrm{MAX}}$, that is, to establish what size of earthquake will not occur (or is unlikely to occur). Therefore, for the entirety of this study we consider the upper bound of the distribution described by Shapiro *et al.* (2010), setting $\chi = 0.95$.

### Seismic Efficiency (Hallo *et al.*, 2014)

McGarr (2014) proposed that the cumulative seismic moment released during injection $\Sigma M_0$ is determined by the total cumulative volume of fluid injected

$$\Sigma M_0 = 2\mu V_T, \quad (4)$$

in which $\mu$ is the rock shear modulus. However, this equation can be considered as a worst-case scenario, where all the strain induced by a volume change is released as seismic energy. In reality, much of the deformation induced by injection will be released aseismically. Hallo *et al.* (2014) therefore define a seismic efficiency ratio $S_{\mathrm{EFF}}$, which describes the ratio of observed cumulative moment release to the theoretical maximum given by $\mu V_T$. Equation (3) is thereby modified to

$$\Sigma M_0 = S_{\mathrm{EFF}} \mu V_T, \quad (5)$$

in which $S_{\mathrm{EFF}}$ can be estimated at a given time from the cumulative moment release and the cumulative injected volume up until this time.

For a given cumulative seismic moment release, size of the largest event will be determined by the $b$-value. Hallo *et al.* (2014) show that $\Sigma M_0$ can be related to the $b$-value, the largest event detected $M_{\mathrm{MAX}}^{\mathrm{M}}$, and the minimum magnitude of completeness $M_{\mathrm{MIN}}$:

$$\Sigma M_0 = \frac{b \times 10^a \times 10^{9.1}}{1.5 - b}\left(10^{(M_{\mathrm{MAX}}^{\mathrm{M}}(1.5-b))} - 10^{(M_{\mathrm{MIN}}(1.5-b))}\right), \quad (6)$$

in which

$$a = bM_{\mathrm{MAX}}^{\mathrm{M}} - \log(10^{b\delta} - 10^{-b\delta}), \quad (7)$$

and $\delta$ is the probabilistic half-bin size defined around $M_{\mathrm{MAX}}^{\mathrm{M}}$, as described by Hallo *et al.* (2014). Based on equation (5), we can determine the total expected $\Sigma M_0$ based on the observed seismic efficiency $S_{\mathrm{EFF}}$ and the planned total injection volume $V_T$. Once we have estimated $\Sigma M_0$, we invert equa-

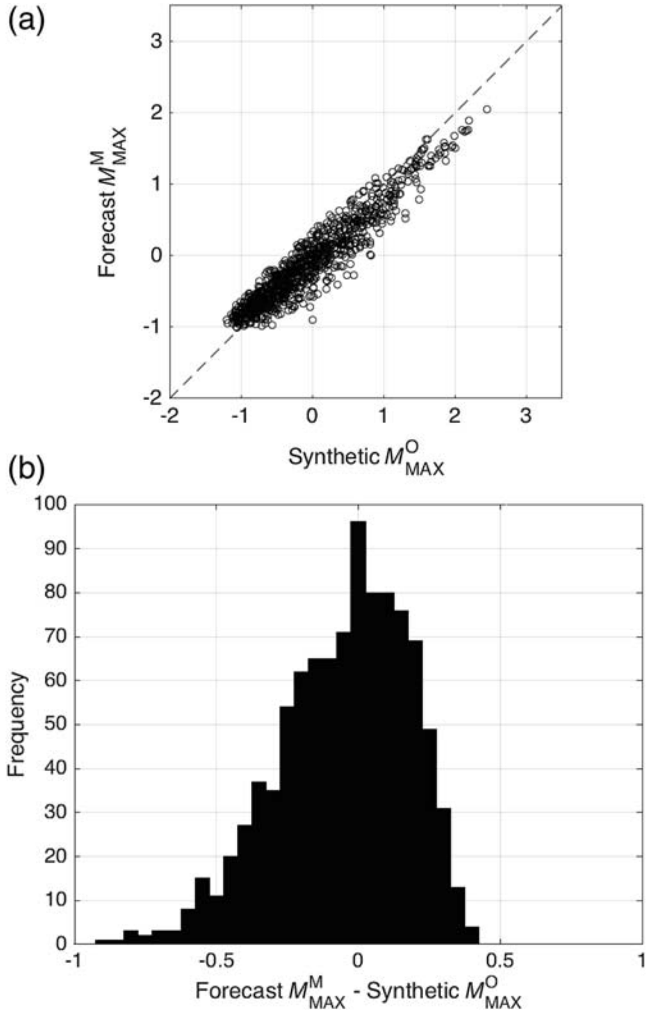


**Figure 3.** Numerical evaluation of the uncertainties inherent when using equations (6) and (7) to forecast $M_{MAX}$. A modeled population of events is sampled from a Gutenberg and Richter (1944) distribution. $M_{MAX}$ is forecast and compared with the largest event in the simulated population. In (a), we compare the synthetic and forecast values, whereas in (b) we show a histogram of the differences between the forecast and modeled values.

tions (6) and (7) to forecast $M^M_{MAX}$ based on the observed $b$-values. Essentially, $M^M_{MAX}$ is a function of the seismic efficiency, which describes how much seismic moment is released per unit volume injected, and the $b$-value, which describes whether this seismic moment is released as a few large events or as many small events.

Whereas the Shapiro *et al.* (2010) $S_I$ method provides a probability distribution for $M_{MAX}$ (equation 3), the Hallo *et al.* (2014) method provides a single estimate for $M^M_{MAX}$ based on the observed (or forecast) $b$ and $S_{EFF}$ values. As such, assuming the Hallo *et al.* method is a true representation of the induced seismicity, random variability alone would mean that the actual $M^O_{MAX}$ value would be larger than the model for half the cases. As described above, our goal is to establish conservative $M^M_{MAX}$ values, whereby we have confidence that no events larger than $M^M_{MAX}$ will occur. Therefore, we require a value based on equations (6) and (7) that also take into account uncertainties inherent in the approach.

To do this, we consider synthetic, stochastically generated event populations. By randomly sampling from a G-R distribution, we generate event populations with a given $b$-value and $\Sigma M_0$ chosen randomly from $0.8 < b < 3.5$ and $9 < \log_{10} \Sigma M_O < 14$. We then compare the largest sampled event (which we refer to as the synthetic $M^O_{MAX}$) with the forecast from the given $b$ and $\Sigma M_0$ values using equations (6) and (7) (the forecast $M^M_{MAX}$). Our results for 1000 such realizations are shown in Figure 3. We find that for 98% of model realizations, the forecast value of $M^M_{MAX}$ is within 0.5 magnitude units of the synthetic $M^O_{MAX}$. Because we are primarily concerned with setting a conservative envelope that is not exceeded, in the Results section we take as $M^M_{MAX}$ the value computed using the Hallo *et al.* (2014) method (equations 6 and 7) $+0.5$.

There is currently some debate as to whether there really is a link between injection volume and the rate and/or size of induced earthquakes (e.g., Atkinson *et al.*, 2016; van der Elst *et al.*, 2016). This debate stems from fundamental questions as to the nature of rupture mechanics during induced seismicity. Gischig (2015) describes two end members for rupture behavior. In the first case, rupture may initiate within the zone of increased pressure, but uncontrolled rupture can continue along faults outside of this zone, releasing tectonically accumulated strain energy. Event size will be therefore determined by tectonic factors such as fault dimensions and *in situ* stress conditions. In the second case, the rupture is spatially limited to the zone of increased pore pressure, in which case the injection volume places an *a priori* deterministic limit on the maximum event size.

The second case, where the injection volume places a deterministic limit on event size, is often characterized by the McGarr (2014) limit (equation 4). However, observations of events that appear to breach this limit (e.g., Atkinson *et al.*, 2016) indicate that, at least in certain cases, the first of the Gischig (2015) end members applies. Therefore, an *a priori* deterministic limit on event size cannot be assumed based on injection volume.

However, in our approach there is no requirement that $S_{EFF} \leq 1$, and therefore there is no *a priori* deterministic limit to event size. If $S_{EFF} > 1$, this indicates that the cumulative moment released is larger than the strain energy introduced by injection, and therefore the tectonically accumulated strain energy is also being released. Equation (5) requires simply that there is proportionality between $V_T$ and $\Sigma M_0$, in which $S_{EFF}$ is to be determined by observation for a given site. Van der Elst *et al.* (2016) examined a range of case studies to investigate whether the number of earthquakes induced during injection is proportional to injection volume, and found strong evidence that this was indeed the case, with the implication that the event nucleation rate is controlled by the injection volume. If $b$-values are constant, then this implies that the cumulative moment release will also be proportional to injection volume.

## Application to Microseismic Data

To compute $b$-values, we use the maximum-likelihood approach described by Aki (1965). To estimate $M_{MIN}$, we follow the method described by Clauset *et al.* (2009) to assess the quality of fit between the observed EMD and the G-R relationship using a Kolmogorov–Smirnov test, choosing as $M_{MIN}$ the smallest magnitude at which the null hypothesis (that the observed distribution can be modeled by the G-R relationship) is not rejected at a 10% significance level. Fitting a G-R relationship to an observed EMD can be unreliable for low event numbers. Therefore, we require a minimum of 50 events with magnitudes larger than $M_{MIN}$ for a reliable measurement. This means that our approach will only provide an estimate for $M_{MAX}^{M}$ once sufficient microseismic events have occurred.

Figure 4 shows an example of how we apply these methods to the microseismic datasets. Plots for every stage are available in the Ⓔ electronic supplement to this article. We proceed at intervals of 120 s. After each interval has elapsed, we recalculate the $b$, $S_{EFF}$, and $S_I$ parameters based on the total volume injected and the events recorded up until this time. We then use equations (3), (6), and (7) to estimate, using the Shapiro *et al.* (2010) and Hallo *et al.* (2014) methods, the expected value of $M_{MAX}^{M}$ given the injection volume that is planned to take place during the next 120 s interval.

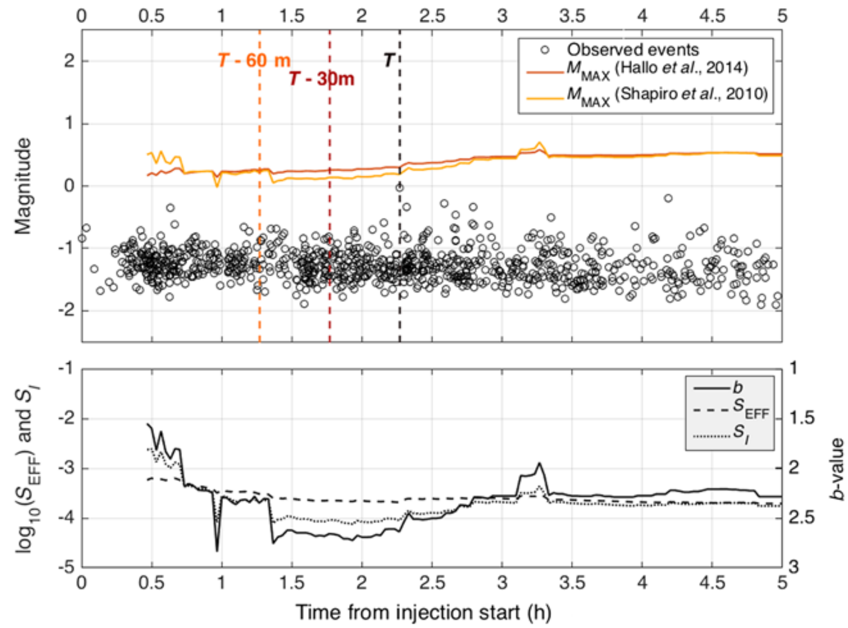


**Figure 4.** Example demonstrating how we forecast $M_{MAX}^{M}$ during an HF stage. In the lower panel, we update $b$, $S_{EFF}$, and $S_I$ during injection. Based on these parameters, we estimate $M_{MAX}^{M}$ using the methods described by Shapiro *et al.* (2010) and Hallo *et al.* (2014), and compare these to the observed event population. The vertical dashed lines in the upper panel represent the $M_{MAX}^{M}$ estimates at the time of the largest event, and 30 and 60 min prior to this event. These data are from stage HR1-A-S10. The color version of this figure is available only in the electronic edition.

In the lower panel of Figure 4, we plot the measured values of $b$, $S_{EFF}$, and $S_I$ with time. In the upper panel of Figure 4, we compare the resulting forecasts of $M_{MAX}^{M}$ with observed event magnitudes. We note that in the example shown in Figure 4, the forecasted largest event size stabilizes at a value of approximately $M_{MAX}^{M} = 0.2$ within 40 min of the start of injection. This is slightly larger than the largest observed event, which has a magnitude of $M_{MAX}^{O} = 0.0$ and occurs 140 min after the start of injection.

In the Results section, we compare $M_{MAX}^{O}$ with the value of $M_{MAX}^{M}$ at the time that the largest event occurred. We also compare $M_{MAX}^{O}$ with $M_{MAX}^{M}$ at a time 60 min and then 30 min before the largest event occurred. We do this to identify the capacity of such methods to provide an opportunity for mitigation by giving an operator sufficient warning to alter (or cease) their stimulation program.

Before considering the results of our method as applied to all stages of both datasets, we note several features from Figure 4. First, we note the similarity between the two curves for $S_I$ and $\log_{10}(S_{EFF})$. This is to be expected given how the two parameters are defined. If $M_{MIN}$ is used as the "$M$" term in equation (3), then the difference $S_I - \log_{10}(S_{EFF})$ will be given by

$$S_I - \log S_{EFF} = \log(N_t(M_{MIN})/V_t) + bM_{MIN} - \log(\Sigma M_O/\mu V_t). \tag{8}$$

Rearranging this equation and substituting $\Sigma M_0 = N_t < M_0 >$, in which $< M_0 >$ is the mean moment release per event, we get

$$S_I - \log S_{EFF} = bM_{MIN} - \log(M_O/\mu). \tag{9}$$

In the case studies presented here, $M_{MIN}$ is typically approximately $-1.5$, $b$ is typically 2, $< M_0 >$ is typically of the order $10^7$ N·m (equivalent to a magnitude of approximately $-1$) and we approximate the shear modulus as $\mu = 20 \times 10^9$ Pa. Hence the similarity in values between $S_I$ and $\log_{10}(S_{EFF})$. We also note that the values of $M_{MAX}^{M}$ computed by the two methods are similar. This gives us confidence that both independent methods provide similar results.

## Results

Before showing the results using the two methods described above, in Figure 5 we compare the observed values for $M_{MAX}^{O}$ for each stage with the values of $M_{MAX}^{M}$ forecast using the McGarr (2014) equation $M_{MAX}^{M} = \mu V_T$. We do this primarily to demonstrate that there does not appear to be any correlation between the observed $M_{MAX}^{O}$ of each stage and the volume injected at the time of occurrence of each event. We also note that the observed magnitudes are far smaller than those estimated by the McGarr (2014) equation.

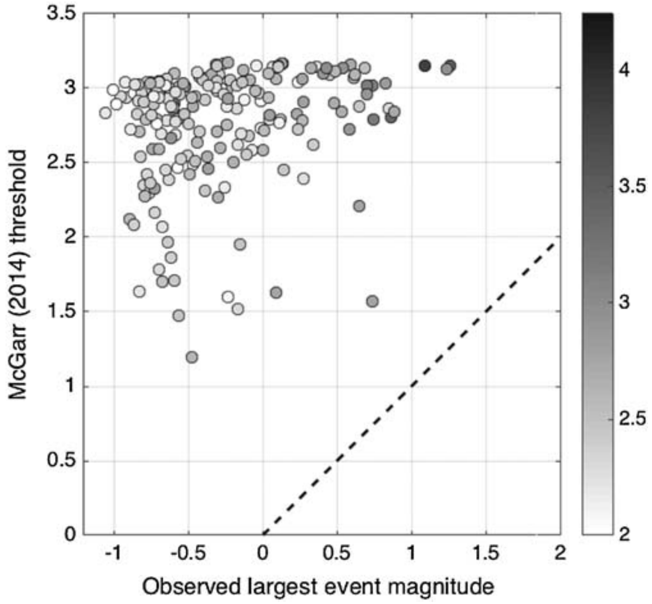


**Figure 5.** Comparison between the observed $M_{MAX}^{O}$ for every stage of both datasets, and that estimated using the McGarr (2014) equation, in which $M_{MAX}^{M}$ is directly determined by the injected volume. Symbols are shaded by $\log_{10}(N)$, in which $N$ is the total number of events per stage. The dashed line indicates a 1:1 ratio.

In Figure 6, we compare the observed and forecast $M_{MAX}$ values using the Hallo *et al.* (2014) method. As per Figure 4, we compare the forecasted $M_{MAX}^{M}$ values at the time that the largest event occurred, but also compare the forecasted $M_{MAX}^{M}$ values 30 and 60 min before the occurrence of the largest event. In Figure 7, we do the same for the Shapiro *et al.* (2010) method.

We note several features from these results. First, as required, in general, $M_{MAX}^{M} \geq M_{MAX}^{O}$ for almost every stage. Not only this, but stages that produced smaller events have smaller values of $M_{MAX}^{M}$, i.e., there is clear correlation between $M_{MAX}^{M}$ and $M_{MAX}^{O}$. This is encouraging, as it implies that these methods do have some forecasting power, unlike the results provided by the McGarr (2014) approach shown in Figure 5. This correlation is present even for the $T - 60$ min measurements, implying that these methods are capable of identifying stages that may induce larger events a significant period of time before such events occur.

There is only one stage, at HR2, where both the Shapiro *et al.* (2010) and Hallo *et al.* (2014) methods significantly underestimate $M_{MAX}^{O}$. We note that this stage had only 131 events in total, making it one of the smallest stages in terms of the number of events. The robustness of statistical techniques such as these will be dependent on the number of events sampled, so it is perhaps unsurprising that stages with fewer events might produce less reliable results.

## Discussion

### Do Seismicity Parameters Vary during Injection Stages?

The models we use to forecast $M_{MAX}^{M}$ are entirely statistical and do not incorporate any geological information.

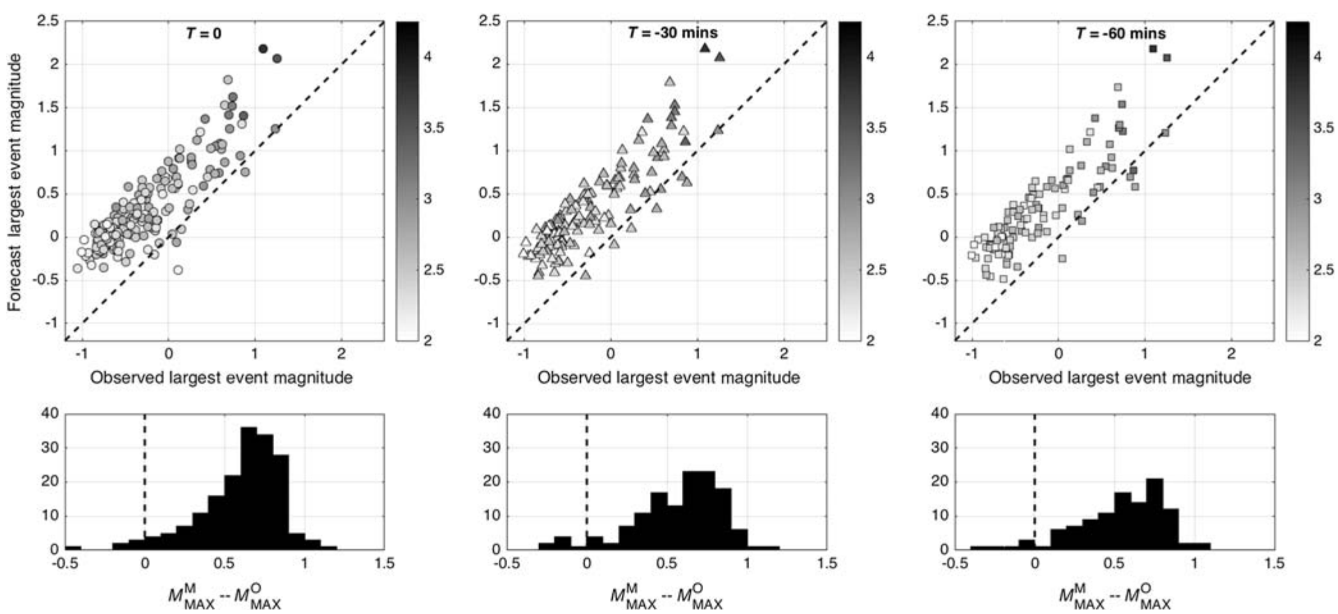


**Figure 6.** Comparison between the observed $M_{MAX}^{O}$ for every stage of both datasets, and that estimated using the Hallo *et al.* (2014) approach. The upper panels show crossplots of observed and modeled $M_{MAX}^{M}$ values, whereas the lower panels show histograms of $M_{MAX}^{M} - M_{MAX}^{O}$. For each case, we show the values of $M_{MAX}^{M}$ at the time that the largest event occurred, and at 30 and 60 min prior to this time. The symbols are shaded by $\log_{10}(N)$, in which $N$ is the total number of events per stage. The dashed lines in the upper panels represent $M_{MAX}^{O} = M_{MAX}^{M}$. Note that for a handful of stages, robust estimates are only obtained within 30 or 60 min of the largest event. In such cases, no $M_{MAX}^{M}$ value is returned at the $T - 30$ or $T - 60$ cases, and so there are slightly fewer points plotted for these cases.

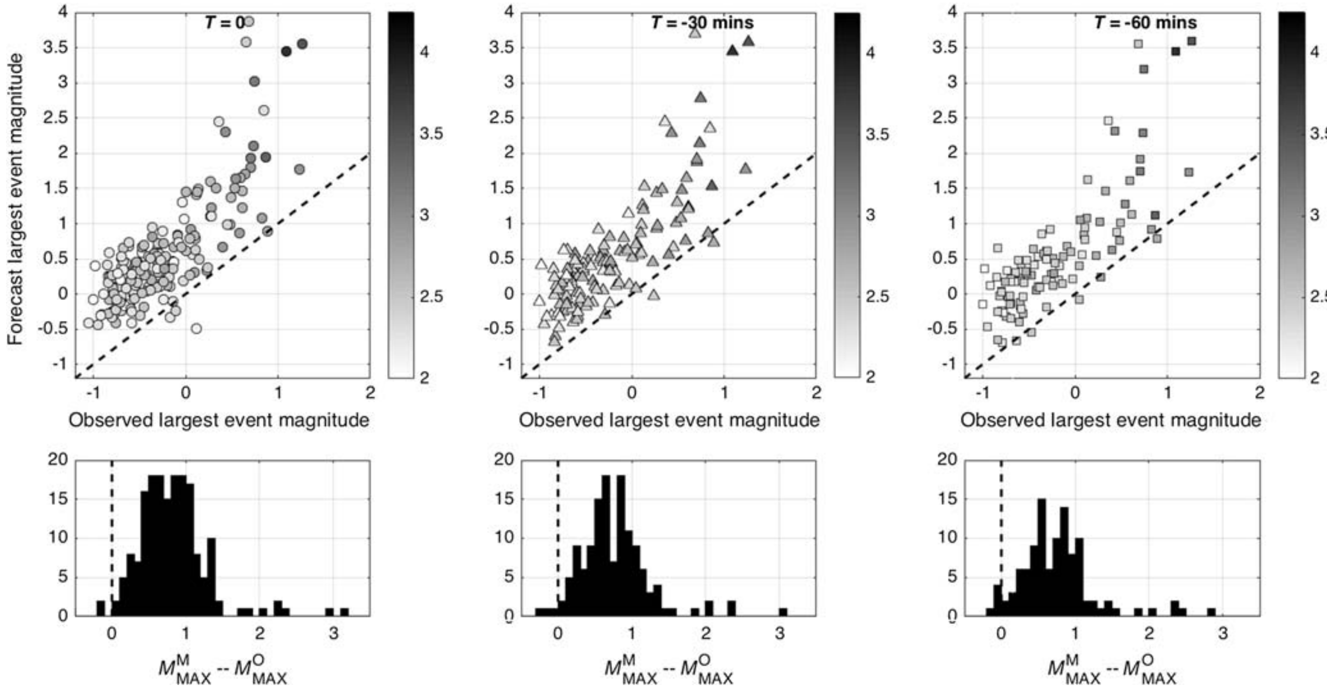


**Figure 7.** Comparison between the observed $M^{O}_{MAX}$ for every stage of both datasets, and that estimated using the Shapiro *et al.* (2010) approach. This figure follows the same format as Figure 6.

The major advantage of these statistical approaches is that they are relatively simple to use (requiring only that the volume injected, and the number and magnitude of seismic events, can be measured). The principal assumption that underpins this type of approach is that both $b$, $S_{EFF}$, and/or $S_I$ will remain consistent throughout the injection period. It is by no means clear that this will always be the case.

These parameters might be affected by a range of factors; including, the *in situ* stress conditions, the lithology of the rock through which hydraulic fractures are propagating, and the presence of pre-existing fracture networks and/or faults. Generally speaking, the volume of rock influenced by injection increases as the pressure front moves out from the injection well. Therefore, the pressure pulse induced by injection may begin to act on different layers and/or structures as injection continues. It is easy to imagine scenarios where a growing hydraulic fracture intersects with a pre-existing fault, or propagates into an underlying or overlying layer that is more seismogenic, resulting in a change in the rate of seismicity and/or $b$-value.

The key question then becomes whether such changes are rapid, or whether there will be a more gradual evolution. If the seismicity changes suddenly, then larger events may occur that cannot be anticipated based on the preceding microseismicity. It would therefore be very difficult for an operator to mitigate induced seismicity, as larger events would occur "out of the blue." In contrast, if such changes occur relatively gradually then an operator may be able to identify an increase in the seismicity rate, or a decrease in the G-R $b$-value, that would indicate an increasing probability of the occurrence of a larger event. If closely monitored, this might allow an operator to take appropriate mitigating action (reducing pumping rates and/or pressures, or indeed ceasing to pump altogether).

Incidentally, this assumption is also implicit in existing schemes that are used to mitigate induced seismicity such as TLSs, although this assumption is rarely stated explicitly. If large events are triggered immediately when an HF intersects a fault, then TLSs will be ineffective, because an event that is much larger than the red-light threshold could occur without any prior TLS-based mitigation actions having been taken. In contrast, if there is a more gradual buildup of seismicity upon intersection between a hydraulic fracture and a fault, then the amber and red lights will progressively be triggered, and the appropriate mitigation steps taken.

We note that both Dinske and Shapiro (2013) and van der Elst *et al.* (2016) observed remarkably constant values of $S_I$ during fluid injection, across a wide variety of settings including HF, stimulation of geothermal reservoirs, and during wastewater disposal. There are also sound physical reasons to expect a gradual increase in seismic magnitudes as a hydraulic fracture impinges on a fault, as opposed to a sudden jump. When a fracture first meets a fault, both the area of the fault is affected and the volume of fluid injected into the fault will be small. As such, we might expect the initial events to be smaller. As injection continues, the area of the fault affected will increase, as will the volume of fluid injected into it, which would be expected to increase the event magnitudes as injection continues.

This assumption is borne out in the results we present here, most notably in the fact that the forecast $M^{M}_{MAX}$ values tend to anticipate the observed largest events by at least 60 min (Figs. 6 and 7). It is also apparent when the evolution of these parameters is examined in detail during each stimulation stage (see Ⓔ electronic supplement). The implication is that large induced events do not occur "out of the blue," but are accompanied by a buildup in seismicity as the stimulation impinges on a pre-existing fault.

### Strategy for Mitigation of Induced Seismicity

Based on the above results, we suggest the following strategy for the mitigation of induced seismicity. Prior to the start of operations, an acceptable threshold for $M_{\mathrm{MAX}}^{\mathrm{M}}$ is set, based on the vulnerability of nearby populations, buildings and infrastructure to seismic activity, and the expected ground motion that would be caused by events of a given size.

In this case, we arbitrarily set our thresholds as $M_{\mathrm{MAX}}^{\mathrm{M}} > 1$. Given the relative lack of buildings, local populations, or infrastructure near to this site, this is a relatively conservative threshold, but nevertheless affords a clear demonstration of the approach. Because the results for the Hallo *et al.* (2014) method show a tighter correlation between $M_{\mathrm{MAX}}^{\mathrm{M}}$ and $M_{\mathrm{MAX}}^{\mathrm{O}}$ (compare to Figs. 6 and 7), we use this approach as our preferred method to compute $M_{\mathrm{MAX}}^{\mathrm{M}}$. If $M_{\mathrm{MAX}}^{\mathrm{M}}$ exceeds this threshold during a stage, then mitigating actions should be taken. In this case, we suggest that the mitigating action would be to cease injection and move on to the next stage.

Based on our results, we divide the stages into three categories: stages where the $M_{\mathrm{MAX}}^{\mathrm{M}} > 1$ threshold is never reached and therefore no mitigation action is indicated (Fig. 8a,b); stages where the $M_{\mathrm{MAX}}^{\mathrm{M}} > 1$ threshold is reached only after the occurrence of the largest observed event (Fig. 8c,d); and stages where the $M_{\mathrm{MAX}}^{\mathrm{M}} > 1$ threshold is reached before the occurrence of the largest event (Fig. 8e,f).

The first category of stages, where the $M_{\mathrm{MAX}}^{\mathrm{M}} > 1$ threshold was not exceeded at any time, is represented in Figure 8a. An example of such a stage is shown in Figure 8b; 159 out of 195 total stages (82%) fall into this category. The circles in Figure 8a show the largest event to occur in each of these stages; the largest event to occur in a stage where the $M_{\mathrm{MAX}}^{\mathrm{M}} > 1$ threshold was not reached had a magnitude $M_{\mathrm{w}}$ 0.4.

The second category of stages is where the $M_{\mathrm{MAX}}^{\mathrm{M}} > 1$ threshold was exceeded but only after the occurrence of the largest event (Fig. 8c). An example of such a stage is shown in Figure 8d: in this stage the largest event, which has a magnitude of $M_{\mathrm{MAX}}^{\mathrm{O}} = 0.58$, occurs after ~1 hr. The $M_{\mathrm{MAX}}^{\mathrm{M}} > 1$ threshold is reached after 2 hrs of injection. Because the threshold is reached after the occurrence of the largest event, any mitigation steps that might have been taken would not affect the size of the largest event to occur during these stages. A total of 16 stages (8%) fall into this category, and $M_{\mathrm{MAX}}^{\mathrm{O}}$ for each of these stages is depicted in Figure 8c. The largest magnitude event to occur during these stages had a magnitude $M_{\mathrm{w}}$ 0.88.

The third category of stages is where the $M_{\mathrm{MAX}}^{\mathrm{M}} > 1$ threshold was exceeded prior to the occurrence of the largest event. An example of such a stage is shown in Figure 8f: in this stage, the $M_{\mathrm{MAX}}^{\mathrm{M}} > 1$ threshold is reached after ~1 hr of injection. This is over 2.5 hrs before the occurrence of the largest event, which had a magnitude of $M_{\mathrm{MAX}}^{\mathrm{O}} = 1.24$. In other words, the potential for an $M_{\mathrm{w}} > 1$ event is identifiable at a relatively early point during the stage, and it is therefore possible that actions could have been taken that might have mitigated the occurrence of this event. A total of 20 stages (10%) fall into this third category, where the $M_{\mathrm{MAX}}^{\mathrm{M}} > 1$ threshold was reached prior to the occurrence of the largest event. These stages are depicted in Figure 8e, in which the squares indicate the size of the largest event to occur prior to reaching the $M_{\mathrm{MAX}}^{\mathrm{M}} > 1$ threshold, whereas triangles indicate the eventual largest event to occur. Within this category of stages, three had events with magnitudes larger than $M_{\mathrm{w}}$ 1. However, the largest event to occur before reaching the $M_{\mathrm{MAX}}^{\mathrm{M}} > 1$ threshold had a magnitude $M_{\mathrm{w}}$ 0.65.

Overall, we note that for all the stages where the largest event was smaller than $M_{\mathrm{MAX}}^{\mathrm{O}} < 0$, no mitigation actions were indicated. For some stages $0 < M_{\mathrm{w}} < 1$ mitigation actions were indicated, whereas in others they were not. For all the stages where the largest event exceeded $M_{\mathrm{MAX}}^{\mathrm{O}} > 1$, mitigation actions were always indicated prior to the occurrence of these events. The result is that for our mitigated population there are no stages where the largest event exceeds $M_{\mathrm{w}} > 1$.

### Mitigating Actions and Postinjection Seismicity

The major caveat that applied to the results described above is the assumption that ceasing injection can prevent the subsequent larger events from happening. In reality, injection was not stopped, and so we cannot know whether cessation of injection during a stage would actually have mitigated the larger events that occurred later in the stage. In other cases of induced seismicity, events have continued with increasing magnitudes even after injection had ceased (e.g., Häring *et al.*, 2008). It is certainly possible that this would have been the case at this site. Therefore, it is not possible to definitively conclude that, even if mitigation steps had been taken, further seismicity would not have occurred. Nevertheless, we believe that it is important that operators develop scientific criteria to guide operational decisions with respect to mitigating induced seismicity, and that the results presented here clearly indicate that the methods described in this article do provide such a basis.

## Conclusions

We have presented case studies from two sites where microseismic monitoring has imaged pre-existing faults being activated during HF. We investigate the use of two statistical methods found in the literature (Shapiro *et al.*, 2010; Hallo *et al.*, 2014) to forecast the largest event size that might be

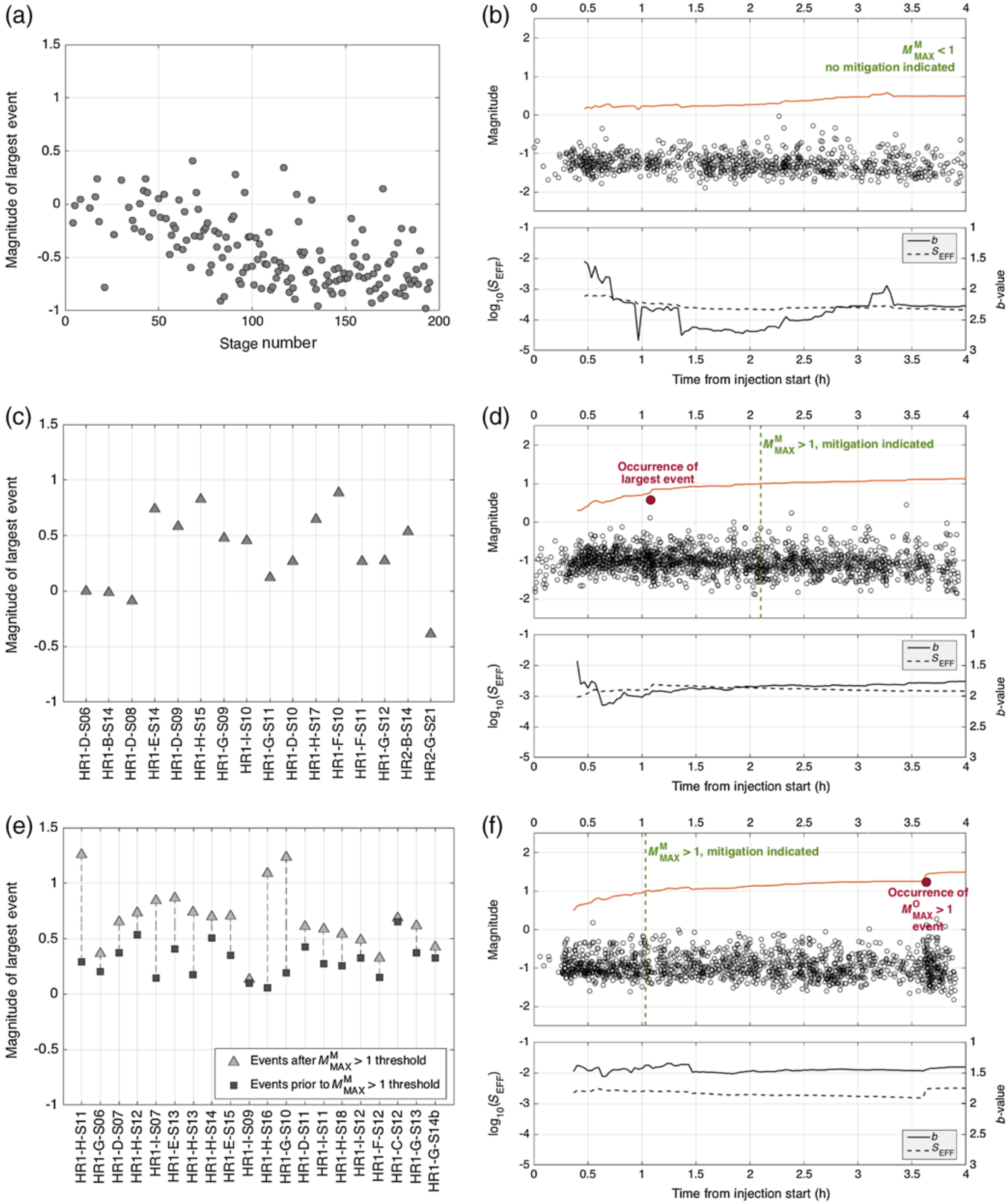


**Figure 8.** Testing the ability of the proposed approach to mitigate induced seismicity. (a) $M^{O}_{MAX}$ for each stage that did not reach the $M^{M}_{MAX} > 1$ threshold. An example of such a stage, where no mitigation actions would have been taken, is shown in (b). (c) $M^{O}_{MAX}$ for each stage that reached the mitigation threshold, but only after the largest event had occurred. In such cases, any mitigation steps would not affect $M^{O}_{MAX}$ (because the largest event has already occurred). (d) An example of such a stage; (e) $M^{O}_{MAX}$ for each stage that reached the $M^{M}_{MAX} > 1$ threshold prior to the occurrence of $M^{O}_{MAX}$. The triangles show the values of $M^{O}_{MAX}$ that actually occurred. The squares show the largest event that occurred prior to reaching the threshold. (f) An example of such a stage. The color version of this figure is available only in the electronic edition.

expected during an HF stage. The basis of these two methods is to characterize the rate of seismicity with respect to the injection volume, and thereby extrapolate to an expected event distribution once the planned total volume has been injected.

Rather than examining these case studies *post hoc*, we explore the potential of these methods to work in a prospective manner: at each given timestep, we only make use of information that is available prior to this time. We do this to put ourselves in the shoes of an operator or regulator, where decisions must be taken in real time as injection proceeds. We find that the proposed methods can forecast the largest event magnitudes with a reasonable degree of accuracy. This enables us to propose a strategy to mitigate HF-IS, whereby alterations to the injection strategy should be made if $M_{\mathrm{MAX}}^{\mathrm{M}}$ exceeds a given threshold. We show that this strategy may have been able to mitigate the larger events that occurred at our case study sites.

The underlying assumption for these methods is that the rate of seismicity with respect to the injection volume will not alter during injection, or that if a fault is encountered, it will evolve gradually, allowing mitigation actions to be taken if real-time monitoring is used. We find that this assumption appears to hold for the datasets considered here. However, further study is required to examine whether this is the case more generally. This highlights the need for good-quality seismic monitoring if the science around injection-induced seismicity is to advance. In many of the most well-known case examples, local monitoring arrays were only installed after the largest events had occurred. It is therefore difficult to determine with any certainty what happened in the time leading up to the triggering, and whether an operator could have made observations that in turn might have allowed them to take mitigating actions.

The most effective types of monitoring systems are either downhole arrays (e.g., Maxwell *et al.*, 2010), as per both case studies in this article, or very large very dense surface arrays, over which data are migrated and stacked (e.g., Chambers *et al.*, 2010). Unfortunately, the costs of these types of deployment are high, and it is unlikely that such systems will be deployed at every injection project. However, novel processing methods using smaller arrays of seismometers placed at the surface (e.g., Skoumal *et al.*, 2015; Verdon *et al.*, 2017) are used to improve the quality of datasets available.

Injection-induced seismicity is a growing concern for various industries, and regulators are increasingly requiring operators to deploy monitoring arrays, usually to meet a TLS requirement of some form. We anticipate that, as more case studies become available, our understanding of injection-induced seismicity will grow, and our ability to mitigate such events will thereby improve.

## Data and Resources

The datasets presented in this article were acquired by the operating company and are proprietary. Therefore, they cannot be released to the public.

## Acknowledgments

The authors would like to thank the operator of the Horn River sites for allowing us to access the data, and to acknowledge ESG Solutions Ltd., the microseismic service provider who processed the dataset. The authors would also like to thank the sponsors of the Bristol University Microseismicity Project (BUMPS), under whose auspices this work was performed.

## References

Aki, K. (1965). Maximum likelihood estimate of $b$ in the formula $\log N = a - bM$ and its confidence limits, *Bull. Earthq. Res. Inst.* **43,** 237–239.

Atkinson, G. M., D. W. Eaton, H. Ghofrani, D. Walker, B. Cheadle, R. Schultz, R. Shcherbakov, K. Tiampo, J. Gu, R. M. Harrington, *et al.* (2016). Hydraulic fracturing and seismicity in the western Canada Sedimentary basin, *Seismol. Res. Lett.* **87,** 1–17.

Bao, X., and D. W. Eaton (2016). Fault activation by hydraulic fracturing in western Canada, *Science* doi: 10.1126/science.aag2583 (in press).

B.C. Oil and Gas Commission (2012). *Investigation of Observed Seismicity in the Horn River Basin*, available at http://www.bcogc.ca/node/8046/ (last accessed July 2015).

B.C. Oil and Gas Commission (2014). *Investigation of Observed Seismicity in the Montney Trend*, available at https://www.bcogc.ca/node/12291/ (last accessed July 2015).

Chambers, K., J.-M. Kendall, S. Brandsberg-Dahl, and J. Rueda (2010). Testing the ability of surface arrays to monitor microseismic activity, *Geophys. Prospect.* **58,** 821–830.

Clarke, H., L. Eisner, P. Styles, and P. Turner (2014). Felt seismicity associated with shale gas hydraulic fracturing: The first documented example in Europe, *Geophys. Res. Lett.* **41,** 8308–8314.

Clauset, A., C. R. Shalizi, and M. E. J. Newman (2009). Power-law distributions in empirical data, *SIAM Rev.* **51,** 661–703.

Darold, A., A. A. Holland, C. Chen, and A. Youngblood (2014). Preliminary analysis of seismicity near Eagleton 1-29, Carter County, July 2014, *Oklahoma Geol. Soc. Open-File Rept. OF2-2014*.

Dinske, C., and S. A. Shapiro (2013). Seismotectonic state of reservoirs inferred from magnitude distributions of fluid-induced seismicity, *J. Seismol.* **17,** 13–25.

Friberg, P. A., G. M. Besana-Ostman, and I. Dricker (2014). Characterisation of an earthquake sequence triggered by hydraulic fracturing in Harrison County, Ohio, *Seismol. Res. Lett.* **85,** 1295–1307.

Gischig, V. S. (2015). Rupture propagation behavior and the largest possible earthquake induced by fluid injection into deep reservoirs, *Geophys. Res. Lett.* **42,** 7420–7428.

Gupta, H. K. (1985). The present status of reservoir induced seismicity investigations with special emphasis on Koyna earthquakes, *Tectonophysics* **118,** 257–279.

Gutenberg, B., and C. F. Richter (1944). Frequency of earthquakes in California, *Bull. Seismol. Soc. Am.* **34,** 185–188.

Hajati, T., C. Langenbruch, and S. A. Shapiro (2015). A statistical model for seismic hazard assessment of hydraulic-fracturing-induced seismicity, *Geophys. Res. Lett.* **42,** 10,601–10,606.

Hakimhashemi, A. H., M. Schoenball, O. Heidbach, A. Zang, and G. Grünthal (2014). Forward modelling of seismicity rate changes in georeservoirs with a hybrid geomechanical-statistical prototype model, *Geothermics* **52,** 185–194.

Hallo, M., I. Oprsal, L. Eisner, and M. Y. Ali (2014). Prediction of magnitude of the largest potentially induced seismic event, *J. Seismol.* **18,** 421–431.

Häring, M. O., U. Schanz, F. Ladner, and B. C. Dyer (2008). Characterisation of the Basel 1 enhanced geothermal system, *Geothermics* **37,** 469–495.

Keranen, K. M., H. M. Savage, G. A. Abers, and E. S. Cochran (2013). Potentially induced earthquakes in Oklahoma, USA: Links between wastewater injection and the 2011 $M_{\mathrm{w}}$ 5.7 earthquake sequence, *Geology* **41,** 699–702.

Langenbruch, C., and M. D. Zoback (2016). How will induced seismicity in Oklahoma respond to decreased saltwater injection rates? *Sci. Adv.* **2,** e1601542, doi: 10.1126/sciadv.1601542.

Li, T., M. F. Cai, and M. Cai (2007). A review of mining-induced seismicity in China, *Int. J. Rock Mech. Min. Sci.* **44,** 1149–1171.

Maxwell, S. C., J. Rutledge, R. Jones, and M. Fehler (2010). Petroleum reservoir characterization using downhole microseismic monitoring, *Geophysics* **75,** A129–A137.

Maxwell, S. C., F. Zhang, and B. Damjanac (2015). Geomechanical modeling of induced seismicity resulting from hydraulic fracturing, *The Leading Edge* **34,** 678–683.

McGarr, A. (2014). Maximum magnitude earthquakes induced by fluid injection, *J. Geophys. Res.* **119,** 1008–1019.

Raleigh, C. B., J. H. Healy, and J. D. Bredehoeft (1976). An experiment in earthquake control at Rangely, Colorado, *Science* **191,** 1230–1237.

Schultz, R., S. Mei, D. Pana, V. Stern, Y. J. Gu, A. Kim, and D. Eaton (2015). The Cardston earthquake swarm and hydraulic fracturing of the Exshaw Formation (Alberta Bakken play), *Bull. Seismol. Soc. Am.* **105,** 2871–2884.

Schultz, R., V. Stern, M. Novakovic, G. Atkinson, and Y. J. Gu (2015). Hydraulic fracturing and the Crooked Lake sequences: Insights gleaned from regional seismic networks, *Geophys. Res. Lett.* **42,** 2750–2758.

Segall, P. (1989). Earthquakes triggered by fluid extraction, *Geology* **17,** 942–946.

Shapiro, S. A., C. Dinske, and C. Langenbruch (2010). Seismogenic index and magnitude probability of earthquakes induced during reservoir fluid stimulations, *The Leading Edge* **29,** 304–309.

Skoumal, R. J., M. R. Brudzinski, and B. S. Currie (2015). Induced earthquakes during hydraulic fracturing in Poland Township, Ohio, *Bull. Seismol. Soc. Am.* **105,** 189–197.

Stork, A. L., J. P. Verdon, and J.-M. Kendall (2014). Assessing the effect of microseismic processing methods on seismic moment and magnitude calculations, *Geophys. Prospect.* **62,** 862–878.

Stork, A. L., J. P. Verdon, and J.-M. Kendall (2015). The microseismic response at the In Salah carbon capture and storage (CCS) site, *Int. J. Greenh. Gas Control* **32,** 159–171.

van der Elst, N. J., M. T. Page, D. A. Weiser, T. H. W. Goebel, and S. M. Hosseini (2016). Induced earthquake magnitudes are as large as (statistically) expected, *J. Geophys. Res.* **121,** 4575–4590.

Verdon, J. P., J.-M. Kendall, S. P. Hicks, and P. Hill (2017). Using beamforming to maximise the detection capability of broadband seismometer arrays deployed to monitor oilfield activities, *Geophys. Prospect.* **65,** 1582–1596.

Verdon, J. P., A. L. Stork, R. C. Bissell, C. E. Bond, and M. J. Werner (2015). Simulation of seismic events induced by $CO_2$ injection at In Salah, Algeria, *Earth Planet. Sci. Lett.* **426,** 118–129.

Wang, R., Y. J. Gu, R. Schultz, A. Kim, and G. Atkinson (2016). Source analysis of a potential hydraulic-fracturing-induced earthquake near Fox Creek, Alberta, *Geophys. Res. Lett.* **43,** 564–573.

Yoon, J. S., A. Zang, and O. Stephansson (2014). Numerical investigation on optimized stimulation of intact and naturally fractured deep geothermal reservoirs using hydro-mechanical coupled discrete particles joints model, *Geothermics* **52,** 165–184.

School of Earth Sciences
University of Bristol
Wills Memorial Building, Queen's Road
Bristol BS8 1RJ, United Kingdom
James.Verdon@bristol.ac.uk
(J.P.V.)

Nexen Energy ULC
801 7th Avenue SW
Calgary, Alberta
Canada T2P 3P7
(J.B.)

Manuscript received 24 July 2017;
Published Online 27 February 2018